Corrosion behavior of 316 stainless steel alloy in high temperature heat storage medium containing oxygen-chloride salt

Le Zhao[1], Jiawei Du[1], Jingyao Wang[1], Xiaoze Du[2,1†], Hongwei Wu[3]

1 Beijing Laboratory of New Energy Storage Technology, North China Electric Power University, Beijing 102206, China

2 School of Energy and Power Engineering, Lanzhou University of Technology, Lanzhou 730050, China

3 School of Physics, Engineering and Computer Science, University of Hertfordshire, Hatfield, AL109AB, UK

Abstract

Understanding the co-adsorption of O and Cl is very important for studying the entire adsorption mechanism of 316 stainless steel (316 SS) alloy corrosion in ternary chloride salts LiCl-KCl-$CaCl_2$. The influence of oxygen on the corrosion behavior of 316 SS alloy in ternary chloride salts is systematically studied through experiments combined with density functional theory (DFT) calculations. Microscopic structural and chemical experimental results indicate that oxygen in the ternary chloride salts accelerates the corrosion of 316 SS alloy. DFT calculations show that the adsorption energy and work function results indicate that as the O coverage increases, electronic transfer becomes more likely on the surface of the 316 SS alloy. Additionally, the changes in the alloy's structure and charge transfer suggest that chemical adsorption has occurred on its surface in the oxygen-containing ternary chloride salts. The charge transfer of different alloying elements

† Corresponding author. Tel.: +86(10)61773923; Fax: +86(10)61773877. Email address: duxz@ncepu.edu.cn (X. Du)

increases in the order of Ni < Fe < Cr. These research findings help in understanding the corrosion mechanism of 316 SS alloy in ternary chloride salts containing impurities under air conditions.

Keywords: first-principles calculations; experiments; corrosion mechanism; impurities

25 **Nomenclature**

E	The adsorption energy, eV
ρ	The charge density, $e \cdot Å^{-3}$

26 *Subscript*

ads	The total of the adsorbates
ads/sub	The slab covered with adsorbates
slab	The relaxed FeCrNi alloy slab

27 *Abbreviation*

AFM	Atomic Force Microscopy
CSP	Concentrated solar power
DFT	Density functional theory
EDS	Energy dispersed X-ray spectroscopy
GGA	Generalized gradient approximation
PAW	Projector augmented wave
PBE	Perdew-Burke-Ernzerhof
SEM	Scanning Electron Microscopy
UPS	Ultraviolet photoelectron spectroscopy
VASP	Vienna ab-initio software package
vdW	van der Waa
XPS	X-ray Photoelectron Spectroscopy
XRD	X-ray diffractometer

28

1. Introduction

Chloride salt, as a heat storage medium, not only has a low cost and large melting latent heat but also offers a high operating temperature range, meeting the needs of high-temperature heat storage for solar energy [1]. However, it is well known that chloride salts can cause corrosion in alloys, and hot corrosion further reduces the service life of superalloys [2-4]. Several methods have been proposed to protect alloys from hot corrosion in molten salt environments, such as protective coatings [5-8] and surface treatments [4, 9, 10].

Generally, the nano-thickness passivation film on metal provides excellent general corrosion resistance. However, it is susceptible to localized corrosion in certain aggressive environments, which can lead to material failure [11]. The FeCrNi alloy is known for its superior corrosion resistance, outstanding comprehensive mechanical properties, and relatively low-cost [12, 13]. As a result, an increasing number of researchers have focused on the FeCrNi alloy in the past few decades. Furthermore, the FeCrNi alloy is considered a potential candidate for high-temperature applications, such as concentrated solar power (CSP) systems [14]. However, the performance and functional life of the FeCrNi alloy in harsh hot corrosion environments still face a long-term challenge [15, 16].

Although a periodic protective oxide film forms between the alloy and the salt, acting as a barrier in the early stages of hot corrosion, some studies suggested that the molten salt environment accelerates both hot corrosion and oxidation of the alloy [17]. Furthermore, some researchers believe that chloride ions can prevent the formation of a protective oxide layer, leading to increased attack in the oxidizing environment [18]. Mansfeld et al. [19] studied the compatibility between molten salt and alloy, finding that molten NaCl erodes alloys along the grain boundary. The molten NaCl diffuses into the alloy, causing degradation and resulting in severe hot corrosion. Zhang et al. [11] observed

that proton irradiation slows down the intergranular corrosion of Ni-Cr alloy in molten fluoride salt at 650 ºC. They proposed that proton irradiation alone reduces the depth of intracrystalline voids in Cr-infiltrated salt. The gap defects generated by irradiation promote diffusion, which more quickly complements the corrosion injection vacancies of the alloy composition. Although hot corrosion generally has a negative impact in molten salt environments, irradiation has been found to slow down corrosion [20].

Oxidation, dealloying, and impurities are recognized as degradation mechanisms that pose significant threats to the next generation of photothermal power station alloys [21]. These impurities are difficult to completely remove, even after prolonged purification processes. Alkali metal chlorides, in particular, readily absorb moisture from the air to form hydroxides. When the molten salt contains OH^- and dissolves O_2, Eqs. (1)-(3) occur during the corrosion process [22, 23]. Wu et al. [24] found that the oxide film on steel is compromised in an alkaline environment containing Cl^-, which increases the corrosion rate of steel. Freiberg et al. [25] reported that oxyradicals decomposing into O in molten salts, with OH further decomposes into O. Additionally, O_2 dissolved in molten salt also reacts with Cl to form O [15]. While Cl itself does not directly oxidize alloys or contribute to the corrosion of structural materials, it can indirectly influence corrosion through reactions with corrosion products [26].

$$O_2 + 2H_2O + 4e^- \rightarrow 4OH^- \quad (1)$$

$$CaCl_2 + OH^- \rightarrow Ca(\mathrm{OH})_2 + 2Cl^- \quad (2)$$

$$O_2 + 4Cl^- \rightarrow 2O^{2-} + 2Cl_2 \quad (3)$$

The corrosion mechanism of the alloy in chloride melts is notably complex. It is generally regarded as a multi-factor effect, with various reactions coupling to produce different corrosion morphologies.

To date, no studies have specifically examined the mechanism of oxidative ion corrosion in molten chloride salts. Furthermore, studying the failure behavior and complex reaction processes at the microstructure of the alloy surface and the molten salt interface is challenging with traditional experimental techniques due to their limited spatial resolution [27]. Atomic-scale simulation effectively complements experimental techniques, providing detailed insights into local properties and elucidating reaction processes [28]. In high-temperature molten salt environments, O and Cl exist as ions [29], and participate in a series of electrochemical reactions on the alloy surface [22]. In DFT simulations, the algorithm cannot directly assign charges to individual atoms [30]. Consequently, researchers typically use neutral atoms rather than ions to construct computational models [31, 32]. Geometric optimization was performed on the model composed entirely of atoms. However, the distinction between ions and atoms was not considered during the simulation process. Numerous simulation results have demonstrated the feasibility of using atoms as substitutes for real ions in density functional theory (DFT) calculations [33]. This research method has gained widespread recognition, particularly in the study of alloy corrosion [34-36]. In summary, using an all-atom model, where ions are replaced by atoms, is both feasible and widely accepted in DFT simulations [31-36].

Therefore, the contribution of O in ternary chloride salts to the corrosion process of 316 stainless steel (SS) alloy is studied using both experimental and simulation methods. The corrosion of the 316 SS alloy surface by Cl and O in molten salt was confirmed and quantified through a combination of experimental and simulation methods. To investigate the contribution of potential interactions, we first show that varying amounts of $CaCl_2$ affect the O content in the salt. The effects of varying O content in molten chloride on 316 SS alloy are investigated using static immersion tests and additional characterization techniques. By analyzing the morphology and oxide composition of 316 SS alloy,

the corrosion properties of ternary chloride salts with varying O content on the alloy are clarified. Additionally, the adsorption energy, structural properties, and electronic properties of O and Cl co-adsorbed on the surface of 316 SS alloy in molten salt are studied using DFT. These studies provide valuable insights for understanding the structure-activity relationship of molten salts and offer guidance for their design. They also contribute to understanding the corrosion mechanism of the 316 SS alloy in ternary chloride salts containing impurities under atmospheric conditions.

2. Experimental methods and analytical models

2.1 Materials and corrosion experiments

The experimental materials consisted of 316 SS alloy and the prepared ternary chloride salt LiCl-KCl-$CaCl_2$ [37]. Before the experiment, the alloy was cut into 8 × 8 × 3 mm slices and mechanically polished to 2000 mesh using SiC sandpaper. The composition of the 316 SS alloy is provided in Table A1. After being polished with diamond polishing paste, the 316 SS alloy was cleaned with ethanol in an ultrasonic cleaner and naturally dried. No defects were observed in the original (AR) morphology except for some shallow polishing scratches.

The complete experimental procedure is detailed in our previous study [38]. Salts with different oxygen contents were placed in separate crucibles to accurately simulate the corrosion of 316 SS alloy by the two ternary chloride salts. The composition and oxygen content of LiCl-KCl-$CaCl_2$ are provided in Table A2. Then, the two ternary chloride salts were exposed to air via a support under the lid to maintain the chemical stability of the salt.

The 316 SS alloy was fully immersed in a 100 mL Al_2O_3 crucible containing 20.0 g of ternary chloride salt (LiCl-KCl-$CaCl_2$). It was then placed in a muffle furnace, where the temperature was set to 650 ℃ for 72 h to ensure complete contact between the 316 SS alloy and the molten salt

during the corrosion experiment. Afterward, the 316 SS alloy was removed and the surface was cleaned with deionized water.

2.2 Characterization

The surface morphology, chemical composition, and cross-sectional morphologies of corrosion products were observed using Scanning Electron Microscopy (SEM) at 20 kV accelerating voltage. The alloy's corrected surface was sealed with epoxy resin before conducting cross-sectional SEM and EDS tests. The morphology and roughness of the corroded alloy surface were evaluated using Atomic Force Microscopy (AFM). The surface area analyzed by AFM is 3 × 3 μm. The phase constituents of corrosion products were identified by Raman spectroscopy with a 532 nm laser. The binding energy of different elements in the corroded alloy was analyzed using X-ray Photoelectron Spectroscopy (XPS).

2.3 Theoretical details

The DFT calculations were performed using the Vienna Ab-initio Simulation Package (VASP) [39] to investigate the competitive corrosion of 316 SS alloy by corrosive anions. All terms in the Kohn-Sham equation were obtained through approximation and simplification during the DFT process. The electron-ion interaction was modeled using the projector augmented wave (PAW) method [40]. For exchange-correlation, the Perdew-Burke-Ernzerhof (PBE) form of the Generalized Gradient Approximation (GGA) was employed [41, 42]. A plane wave cutoff energy of 600 eV was applied. To account for dispersion forces and van der Waals interactions, the vdW-DFT method was utilized for calculating the co-adsorption of O and Cl atoms [43, 44]. Additionally, the DFT-D3 method, proposed by Grimme et al., was implemented to correct for van der Waals interactions [45].

Adsorption calculations were performed on a six-layer 316 SS alloy (1 1 0) slab. A (4 × 4 × 6)

supercell was constructed to simulate the co-adsorption of O and Cl atoms. The corrosive ions (O and Cl atoms) and top four atomic layers were allowed to relax freely, while the bottom two layers remained fixed. The convergence thresholds for the electronic self-consistent field and atomic forces were set to 1.0×10^{-7} eV and 1.0×10^{-4} eV/Å, respectively, within the current numerical parameters. Charge density distributions were visualized using VESTA software. To eliminate interactions between repeated slabs, the slabs were separated along the C-direction, as depicted in Fig. 1

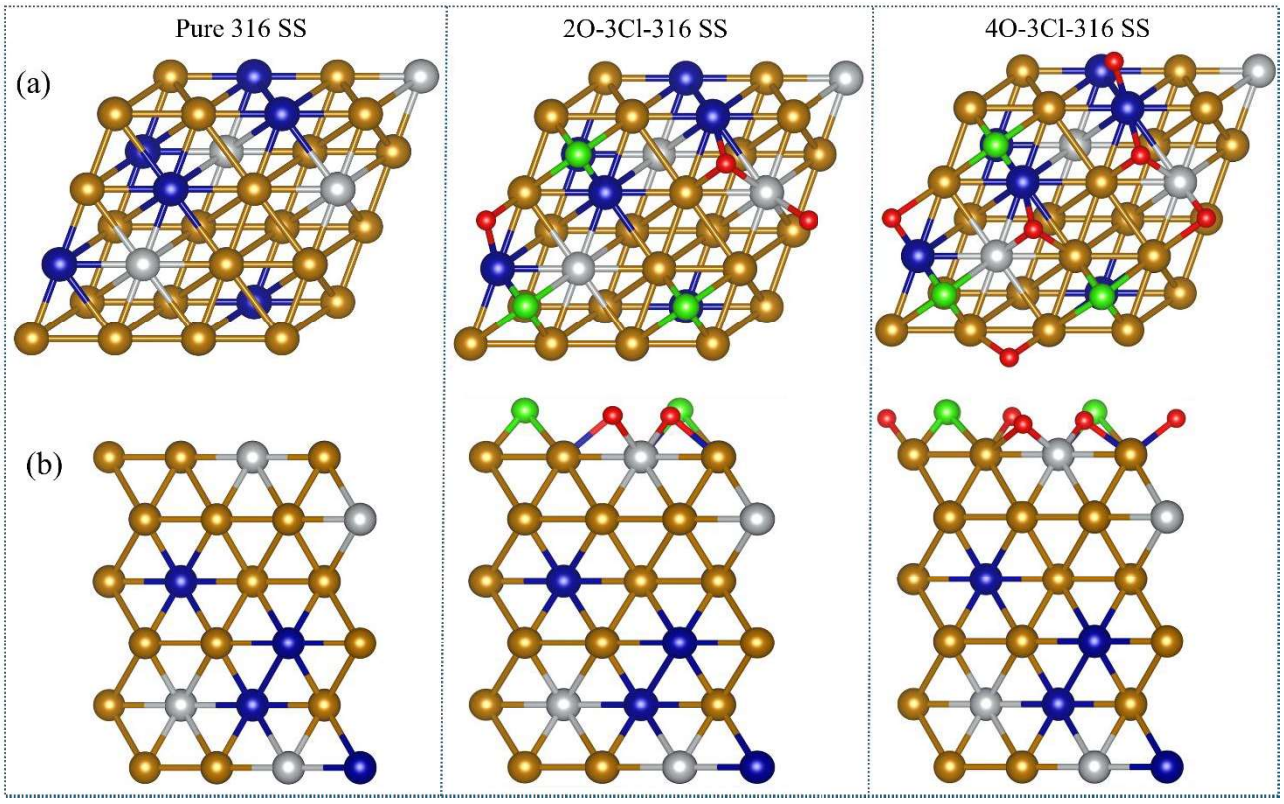

Fig. 1. The adsorption configuration diagram of Cl on the 316 SS alloy with varying O atom. (a) The upper panel is a top view; (b) the lower panel is a side view.

3. Results with analysis

3.1 Morphologies

3.1.1 Surface morphologies

Fig. 2 illustrates the surface morphology of the 316 SS alloy after immersion in various ternary

chloride salts at 650 ℃ for 72 h. The surface morphologies of the samples immersed in molten chloride salts vary significantly depending on the O content. The surface of the 316 SS alloy immersed in salt 1 appears smooth, with only a few protrusions. Overall, the morphology remains relatively flat, although some loose corroded grains are observed on the surface, as shown in Fig. 2(a). When the 316 SS alloy is immersed in salt 2, a double-oxide layer forms on its surface. Particles on the oxide layer are randomly distributed and correspond to a polycrystalline spinel type. These particles are roughly divided into two layers, with those in the outer layer being larger in size and exhibiting superior crystallinity. Following corrosion, numerous deep holes of varying sizes are observed on the surface of the alloy [46]. These deep holes, caused by the adsorption of molten salts, expose the underlying alloy, as shown in Fig. 2(b). The propagation of the oxide film, induced by chlorides, is accelerated, potentially forming short-circuit channels that facilitate the adsorption of corrosive ions [22, 47].

Fig. 2 shows three distinct areas on the alloy surface, labeled EDS 1, EDS 2, and EDS 3, with the elemental content of each phase presented in Table 1. EDS 1 of the 316 SS alloy surface immersed in Salt 1 indicates that the alloy matrix contains Fe, Cr, Ni, and a small amount of O, suggesting minimal corrosion by the molten salt. EDS 2 reveals that the corrosion products formed on the alloy surface consist solely of O and Cr, confirming the formation of Cr-rich spinel, which can partially prevent molten salt corrosion [48]. The shaded area in EDS 3 shows that the Cr content is much higher than that of the Cr-rich spinel, while the Fe and Ni contents are also higher than those of the spinel.

Similarly, when the 316 SS alloy is immersed in salt 2, three distinct regions are observed on its surface. EDS 1 mainly shows spinel containing O and Cr elements. The high oxygen content in salt

2 leads to preferential oxide formation on the alloy, which continuously reacts with corrosive Cl, exposing deeper layers of the alloy matrix. Consequently, the elemental distribution of Fe, Cr, and Ni in EDS 2 becomes more uniform on the surface of the 316 SS. In EDS 3 of the 316 SS alloy immersed in salt 2, the Fe and Ni contents are significantly higher than those in EDS 3 of the alloy immersed in salt 1, while the Cr content is lower.

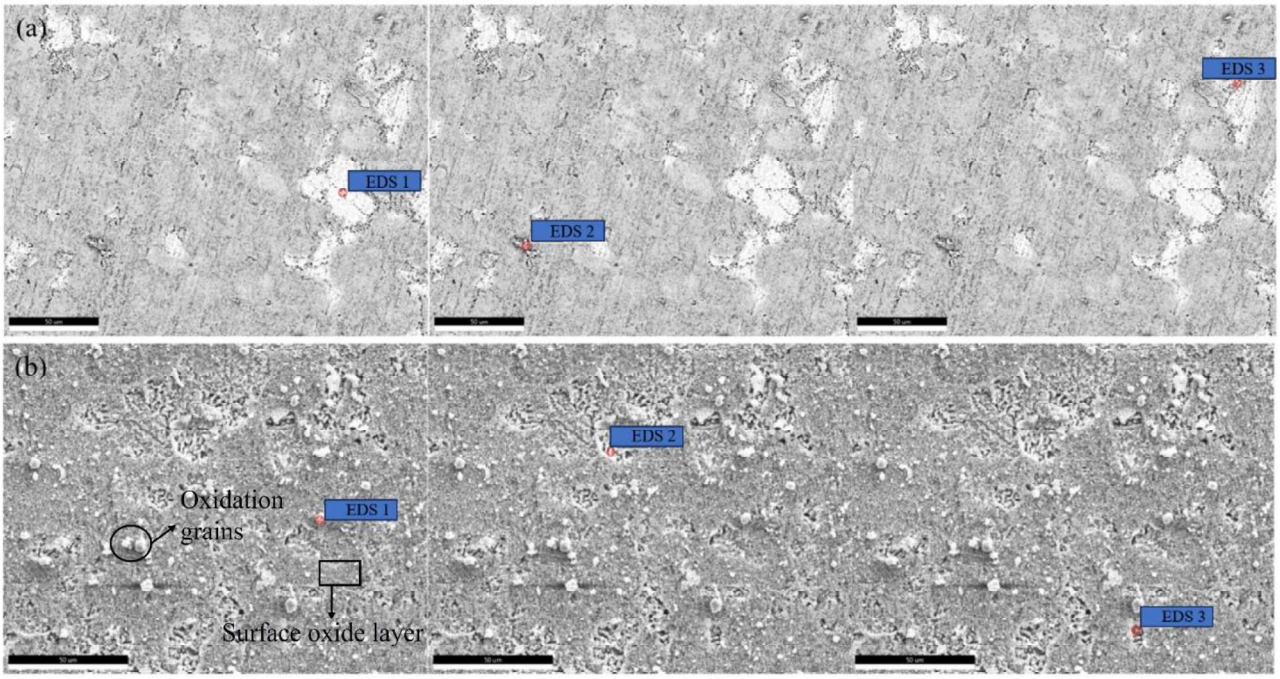

Fig. 2. Surface morphology of the 316 SS alloy after immersion in chloride salts at 650 ºC for 72 h. (a) 316 SS alloy immersed in salt 1; (b) 316 SS alloy immersed in salt 2.

Furthermore, the results in Fig. 2 indicate that the oxide particles distributed on the surface of the oxide scale of the 316 SS alloy immersed in salt 2 are spherical grains. Table 1 shows that these grains are Cr_2O_3, which has been confirmed as a protective layer against corrosion [47]. In summary, the increase in surface grain size of the oxide layer can enhance the corrosion resistance of the 316 SS alloy to molten salts. Unfortunately, the oxide scale formed on the 316 SS alloy immersed in salt 2 exhibits higher porosity than that formed on the alloy immersed in salt 1. The cracks and voids in the

oxide scale may act as pathways for the transport of oxygen and corrosive ions, thereby significantly accelerating the oxidation rate of the alloy.

Table 1. EDS analysis results of 316 SS immersed in molten salts with different O contents as shown in Fig. 2.

Samples	Location	O	Cl	Fe	Cr	Ni
		wt. %				
a	EDS 1	2.5	2.5	36.1	22.9	36.1
	EDS 2	50.0	0.8	0.1	48.6	0.5
	EDS 3	17.9	1.5	1.6	78.4	0.7
b	EDS 1	58.1	0.2	2.2	38.0	1.4
	EDS 2	19.0	0.3	27.8	26.9	26.0
	EDS 3	30.6	0.6	10.2	50.9	7.7

3.1.2 Cross-sectional morphologies

The cross-section of the 316 SS alloy after corrosion was analyzed using scanning electron microscopy. After immersion in two different molten chloride salts for 72 h, the corrosion layer formed in salt 2 is significantly rougher than that in salt 1, as shown in Fig. 3(a) and (b). The oxide layer on the 316 SS alloy, formed in both molten chloride salts, consists of a dealloying layer and ligaments. A dealloying process is observed in the molten chloride salts, and the introduction of O accelerates the dealloying of Fe and Cr from the parent alloy [49, 50]. Over time, the oxide layer evolves into a three-dimensional microporous structure as erosion progresses.

In general, the 316 SS alloy treated with salt 1 forms more ligaments and pores than the alloy treated with salt 2, as shown in Fig. 3(c) and (d). It is speculated that oxygen adsorption, caused by the introduction of higher O content, accelerates the surface coarsening process and reduces the

densification of the oxide film when exposed to salt 2. The oxidation tendency influences the surface mobility of metal atoms in the non-precious alloy. Additionally, the presence of Cr impedes the absorption of O and Cl atoms, making the degradation of Fe oxide more favorable than that of Cr oxide. Moreover, Fig. 3(d) shows that an increase in O leads to intergranular corrosion of the alloy. Additionally, the 316 SS alloy immersed in salt 2 exhibits significant intergranular corrosion, with crack initiation being a crucial stage in the intergranular corrosion cracking process [51]. The surface of the 316 SS alloy readily adsorbs oxygen ions from the air. Due to the high O content in salt 2, the corrosion pits on 316 SS are more numerous compared to those in salt 1, as shown in Fig. 2 and Fig. 4. When Cl concentration is high, surface oxides on the alloy dissolve more readily in chloride salts, forming soluble substances. This dissolution further damages the oxide layer, exposing the alloy matrix to the molten chloride salt environment. The detailed corrosion mechanism is discussed in Section 3.3.

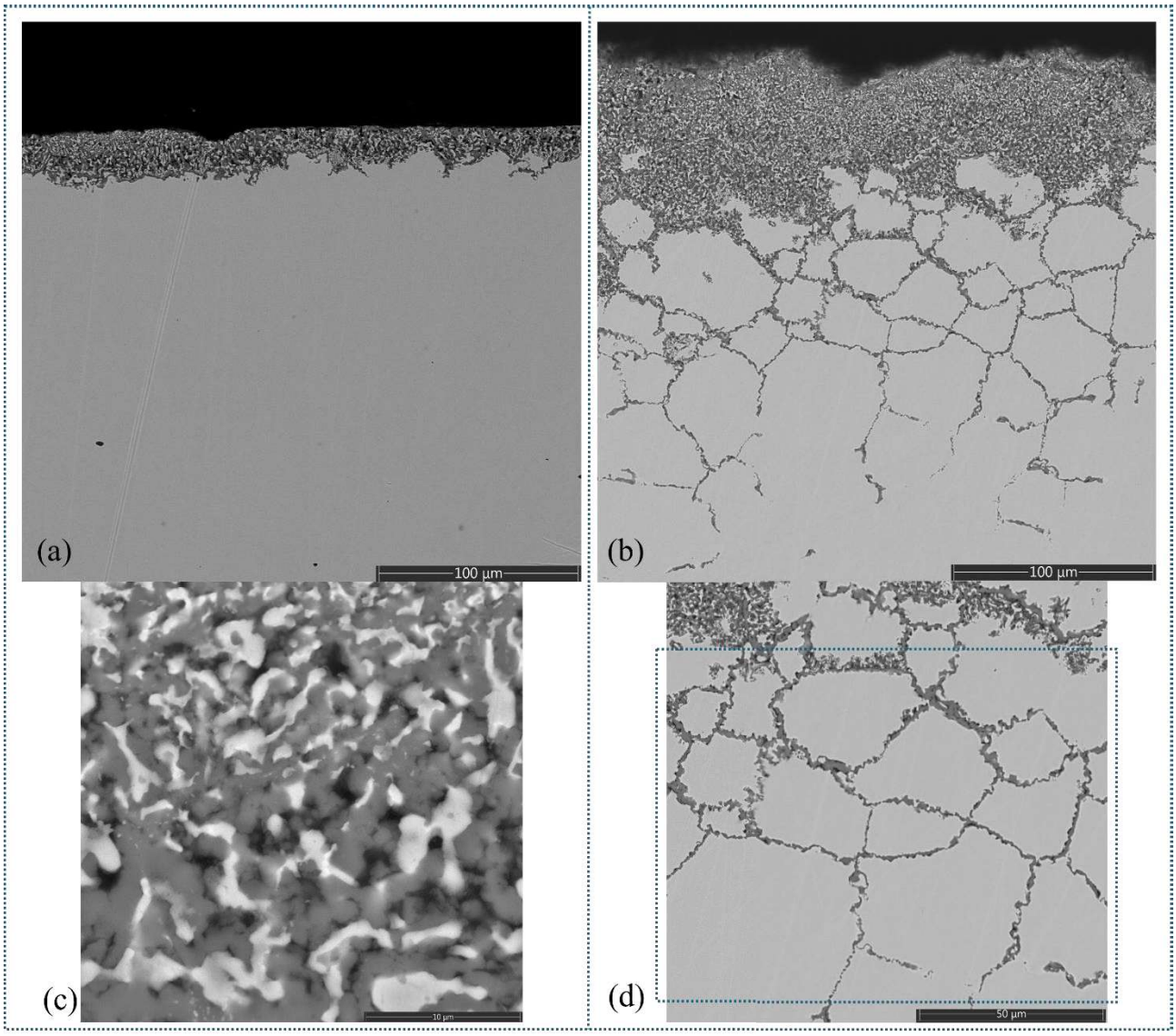

Fig. 3. Cross-sectional micrographs of the 316 SS alloy immersed in different chloride salts at 650 ºC for 72 h. (a) and (c): the 316 SS alloy immersed in salt 1; (b) and (d): the 316 SS alloy immersed in salt 2.

Fig. A1(a) and (b) show the distribution of Fe, Cr, and O elements across the cross-section of the 316 SS alloy. The experimental results reveal a composition of "poor Fe, rich Cr, and rich O" in the corrosion layer, indicating the formation of a dense metal oxide layer on the alloy surface. This oxide layer acts as an effective barrier, preventing the inward diffusion of corrosive anions. The oxide layer formed on the alloy immersed in salt 2 is significantly thicker than that on the alloy immersed in salt

1. Fig. 3(d) illustrates the cross-sectional morphology of the 316 SS alloy after 72 h of immersion in salt 2. Numerous small corrosion pits and deep, inward-propagating cracks are observed, which serve as primary pathways for intergranular corrosion. Together with Fig. 2(b), these observations confirm the occurrence of intergranular corrosion on the surface of the 316 SS alloy when immersed in salt 2. Within most cracks, the concentrations of oxygen and other alloy elements are notably low. As intergranular corrosion progresses, the alloy gradually dissolves into the molten salt. The excessive oxygen content in salt 2 is identified as the primary driver of intergranular corrosion on the 316 SS surface.

3.1.3 3D morphologies

The SEM results were further validated using 3D laser confocal microscopy. Fig. 4 presents 2D and 3D images of the corroded surface of the 316 SS alloy after immersion in different ternary chloride salts. In these images, the blue regions represent areas below the reference surface, while the red regions correspond to areas above it. Distinct differences are observed between the 316 SS alloy immersed in molten salts with varying oxygen contents. The surface of the 316 SS alloy immersed in salt 2 exhibits more severe damage compared to that immersed in salt 1, with an average roughness of 116 nm. The 3D images reveal dispersed oxides of varying heights, resembling mountain-like formations, suggesting localized corrosion [52]. Impurities or secondary phases contribute to the formation of a fragile outer passive layer on the alloy surface. The surface of the alloy exposed to salt 2 contains more passive pits than that exposed to salt 1, consistent with SEM observations. Additionally, the oxide grain boundaries formed in the ternary chloride salt environment are highly susceptible to dissolution, resulting in the formation of small pores that eventually grow into larger pits. These findings indicate that the height variation in the corrosion layer is influenced by the

compactness of the oxide layer.

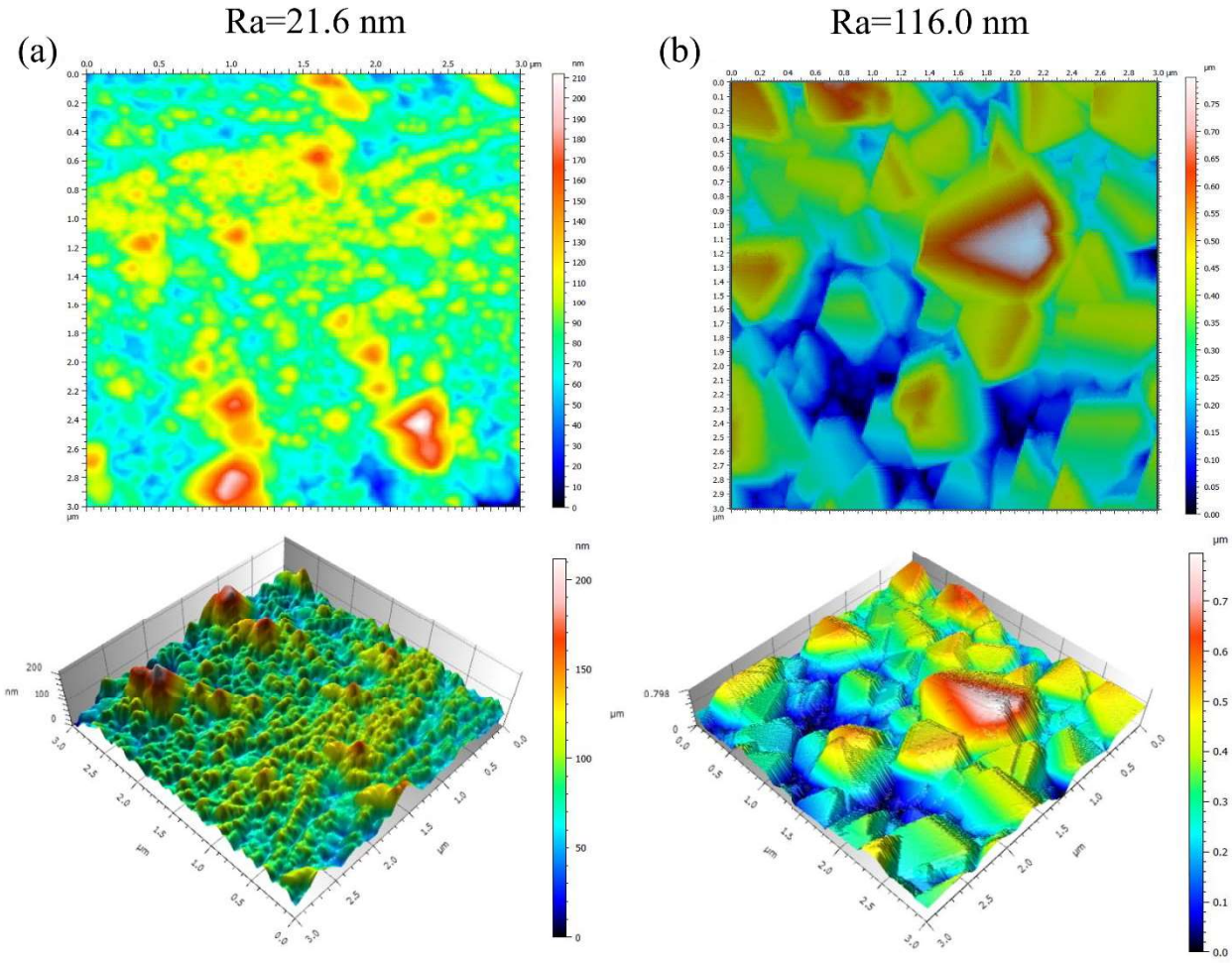

Fig. 4. 2D/3D AFM images for 316 SS alloy immersed in salt 1 and salt 2. (a) 316 SS alloy immersed in salt 1; (b) 316 SS alloy immersed in salt 2.

3.2 Phase components

3.2.1 Raman spectra analysis

Raman spectroscopy was utilized to analyze the composition of the oxide layer on the surface of the 316 SS alloy immersed in molten salts with varying oxygen contents. Using an excitation wavelength of 532 nm, the Raman signal penetrated to a depth of approximately 21.2 nm, capturing oxide-related responses from the alloy surface, as illustrated in Fig. 5. For the alloy immersed in salt 1, two distinct Raman peaks were observed at 447 cm^{-1} and 580 cm^{-1}. The adsorption of oxygen, as

shown in Fig. A1, promotes the formation of an oxide film on the alloy surface. The Raman peak at 447 cm^{-1} corresponds to the bending and symmetric stretching vibrations of Cr and O in $FeCr_2O_4$ [53] and the peak at 580 cm^{-1} is attributed to Fe_2O_3 [54]. Therefore, the Raman spectroscopy results indicate that the corrosion products on the 316 SS alloy immersed in salt 1 include $FeCr_2O_4$ and Fe_2O_3.

Raman spectroscopy reveals two peaks at 440 cm^{-1} and 571 cm^{-1} for the oxide layer formed on the 316 SS alloy immersed in salt 2. Notably, the Raman peaks of the oxide layer for the alloy immersed in salt 2 differ from those observed for salt 1. When the 316 SS alloy was immersed in salt 2, the peak at 571 cm^{-1} corresponds to Cr_2O_3/CrO_3 [18]. For $FeCr_2O_4$, it is often reported in the literature that the peak positions of all Raman bands of chromite can shift by approximately 40 cm^{-1} [53]. Therefore, the $FeCr_2O_4$ on the 316 SS alloy immersed in salt 2 vibrates at 440 cm^{-1}.

The analysis demonstrates that the oxide structure on the 316 SS alloy surface evolves dynamically with increasing oxygen content in the molten salt. Outer iron oxide layers dissolve and detach due to corrosion [55], thereby exposing the underlying chromium-rich oxide layer. The oxide film on the alloy surface forms through a combination of solid-state growth and metal oxide precipitation/dissolution mechanisms [56]. The presence of chromium oxide indicates that the oxide film has decomposed and delaminated. Research suggests that achieving an equilibrium oxide film on the alloy surface requires thousands of hours [57, 58]. The continuous delamination of the oxide film results in significant alterations to the alloy surface.

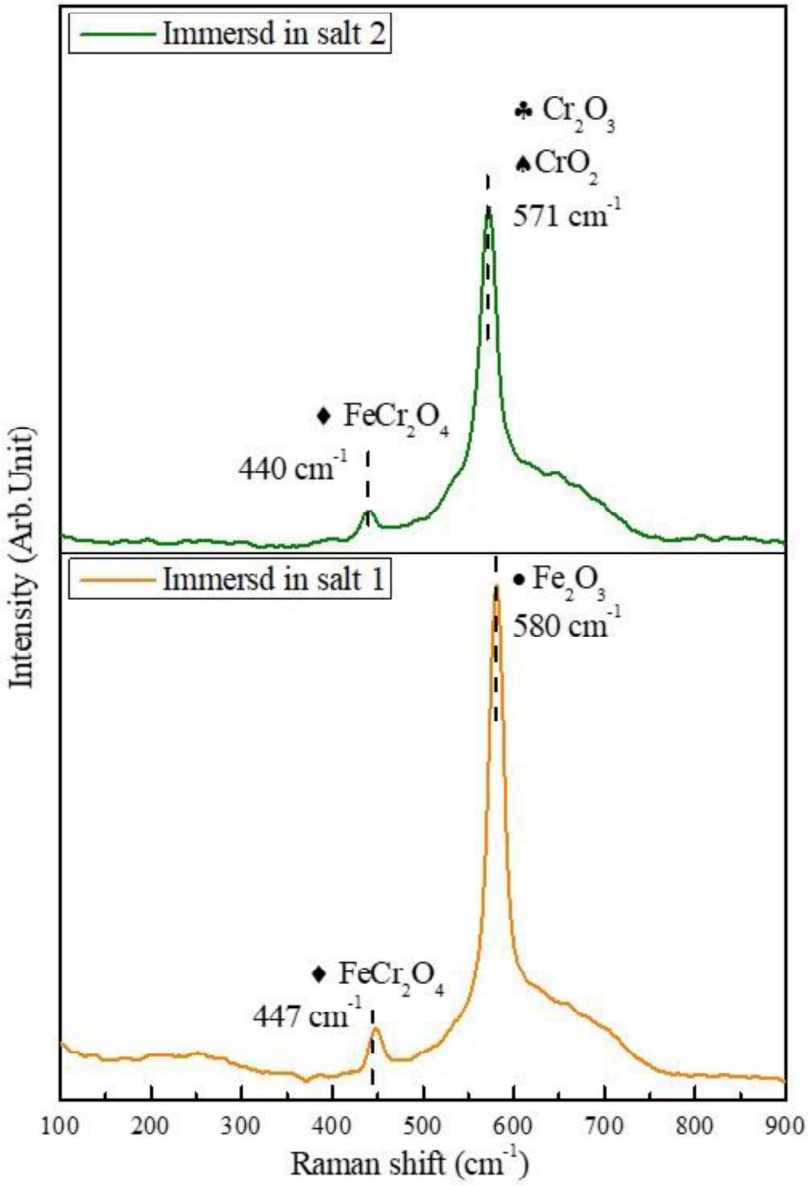

Fig. 5. Raman spectra of 316 SS alloy immersed in different component ternery chloride salts.

3.2.2 XPS analysis

The conventional EDS test is limited in its ability to capture phase information of corrosion products due to the thinness of the corrosion layer on 316 stainless steel (SS). To overcome this, XPS analysis was conducted to determine the chemical valence states of Fe, Ni, Cr, O, and Cl in the alloy's oxide layer, as shown in Fig. 6 and Fig. A2. The 2p3/2 and 2p1/2 spectra were processed using the Shirley algorithm for background subtraction and analyzed using XPSPEAK for peak deconvolution.

The valence states of the elements were identified from the fitted peaks based on the NIST XPS database [59-61]. To further investigate the elemental distribution, the chemical states and distributions of Fe and Cr were analyzed in detail. In the weakly O environment, where oxides and chlorides coexist, Fe was identified in both bivalent (Fe^{2+}) and trivalent (Fe^{3+}) states. The fitted peaks of O1s, Fe2p, Cr2p and Ni2p are shown in Fig. 6, while the fitted peaks of Cl2p are presented in Fig. A2.

According to the XPS spectrum, the surface of the 316 SS alloy immersed in both salts contains metal and oxide components, with Fe^0 and Fe_2O_3 detected [62, 63]. The Cr2p spectra are fitted with double peaks corresponding to the core energy levels of Cr2p3/2 and Cr2p1/2, observed at binding energies of 576.10 eV and 586.02 eV, respectively [64, 65]. According to the NIST database, the first peak corresponds to the M-O bond, indicating the presence of Cr oxides. The second peak corresponds to the M-OH bond, representing Cr oxyhydroxides and hydroxides [66]. This indicates that the passivation layer undergoes chemical modification when the 316 SS alloy is immersed in salt 2, which has a higher oxygen content. The increased signal intensity of Cr oxides and hydroxides suggests a reduction in the Cr content within the oxide layer.

In the Ni2p spectrum, a peak at 852.99 eV corresponds to metallic Ni, while the peaks at 855.47 eV and 874.38 eV are associated with Ni^{2+}, representing the Ni2p3/2 and Ni2p1/2 orbitals, respectively. The formation of nickel oxides and hydroxides on the surface of the 316 SS alloy is attributed to oxidation [67]. The peak at 861.63 eV corresponds to the satellite Ni^{2+}2p3/2 orbital, while the peak at 879.62 eV corresponds to the satellite Ni^{2+}2p1/2 orbital. These peaks are likely caused by the oxidation of Ni on the surface of the 316 SS alloy [68]. These findings are consistent with the results shown in Fig. 7.

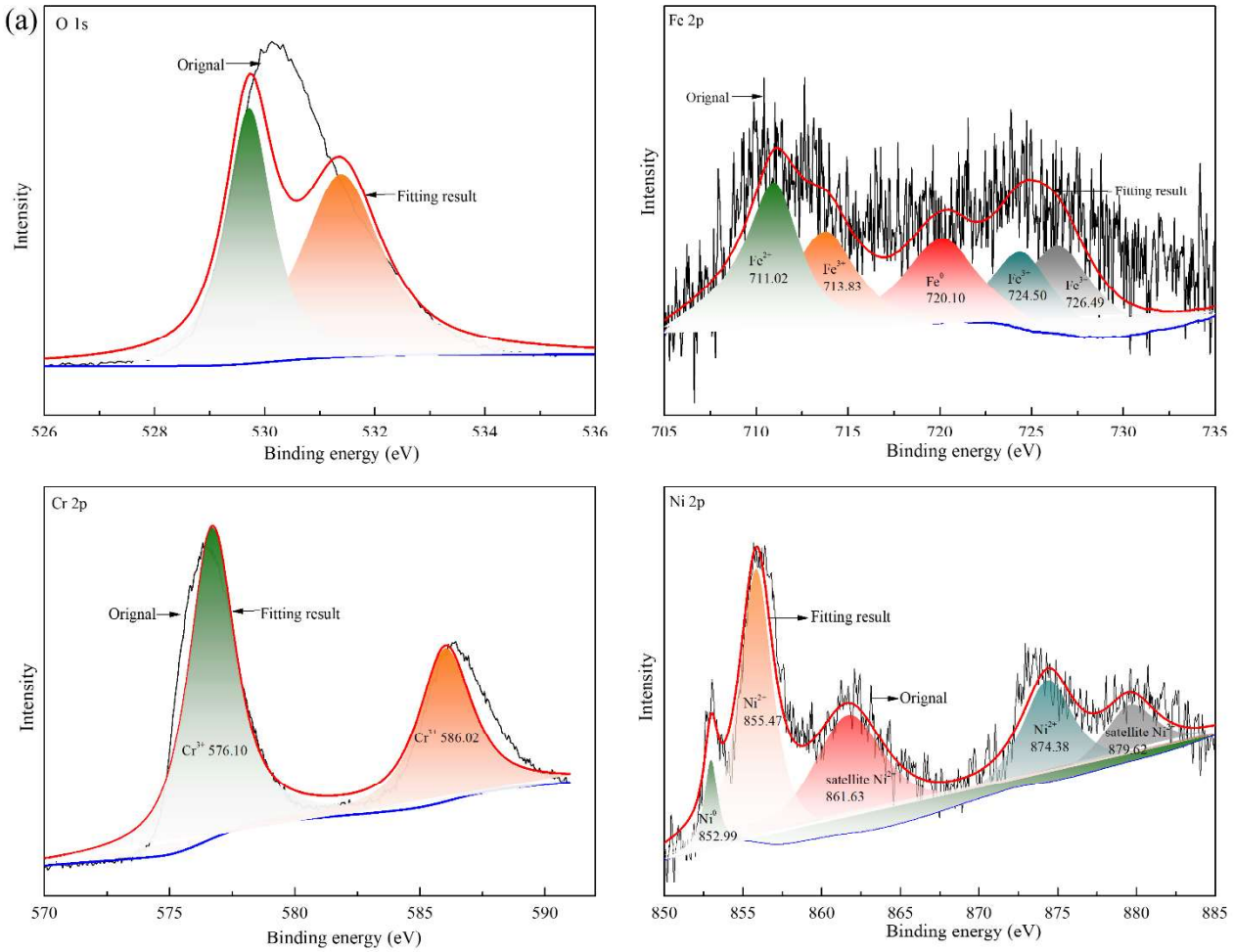
(a)
O 1s
Orignal
Fitting result
Intensity
526
528
530
532
534
536
Binding energy (eV)
Fe 2p
Orignal
Fitting result
Intensity
Fe2+ 711.02
Fe3+ 713.83
Fe0 720.10
Fe3+ 724.50
Fe2+ 726.49
705
710
715
720
725
730
735
Binding energy (eV)
Cr 2p
Orignal
Fitting result
Intensity
Cr3+ 576.10
Cr3+ 586.02
570
575
580
585
590
Binding energy (eV)
Ni 2p
Fitting result
Orignal
Intensity
Ni2+ 855.47
satellite Ni2+ 861.63
Ni0 852.99
Ni2+ 874.38
satellite Ni2+ 879.62
850
855
860
865
870
875
880
885
Binding energy (eV)

305

306

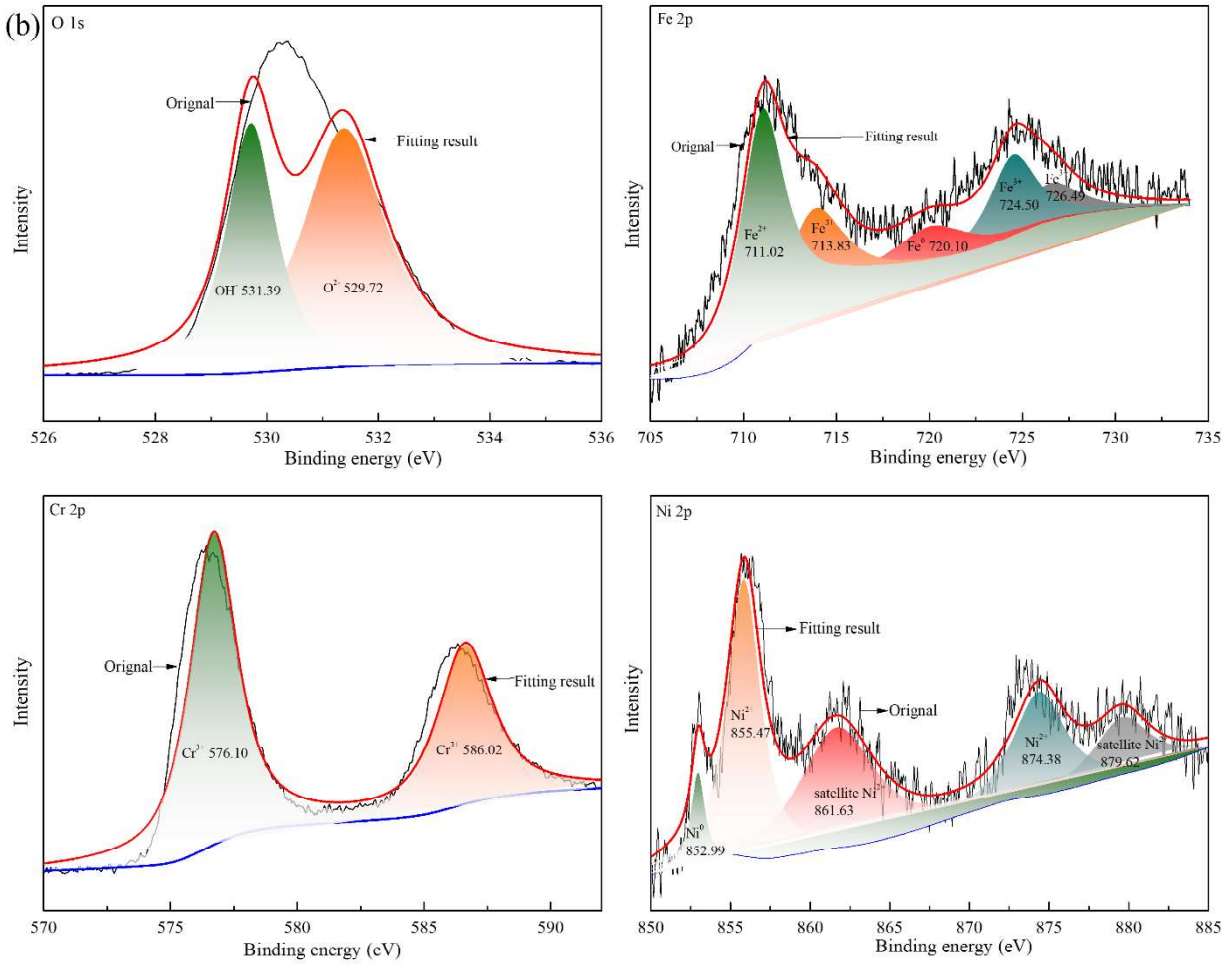

Fig. 6. XPS metal element analysis of the 316 SS alloy after 72 h in salt 1 and salt 2.

For further study, Fig. 7 presents the magnified SEM observations and EDS mapping data of 316 SS alloy at different oxygen contents. The morphology of the 316 SS alloy immersed in salt 1 remains relatively flat and is divided into two colors. The EDS mapping data shows that the surface of the alloy is composed of an oxide layer and an alloy, and the results show that the lighter areas are mainly Fe and Ni. O and Cr are distributed on the darker oxide layer on the alloy surface, and the Cr element tends to be near the oxide layer. By comparing the surface of the 316 SS alloy immersed in salt 1, it is easy to observe that the surface of the alloy immersed in salt 2 is distributed with many deep holes and oxide particles of different sizes. The immersed alloy surface is mainly Fe, Ni and O, and the Cr

element is distributed throughout the alloy surface. In addition, the thin oxide layer formed on the surface of the 316 SS alloy in salt 1 causes the content of Cr_2O_3 to be significantly lower than that in salt 2. In addition, the XPS valence state analysis of Ni and Cr shows that the main oxidation product is Cr_2O_3 regardless of the oxygen content in the molten salt environment.

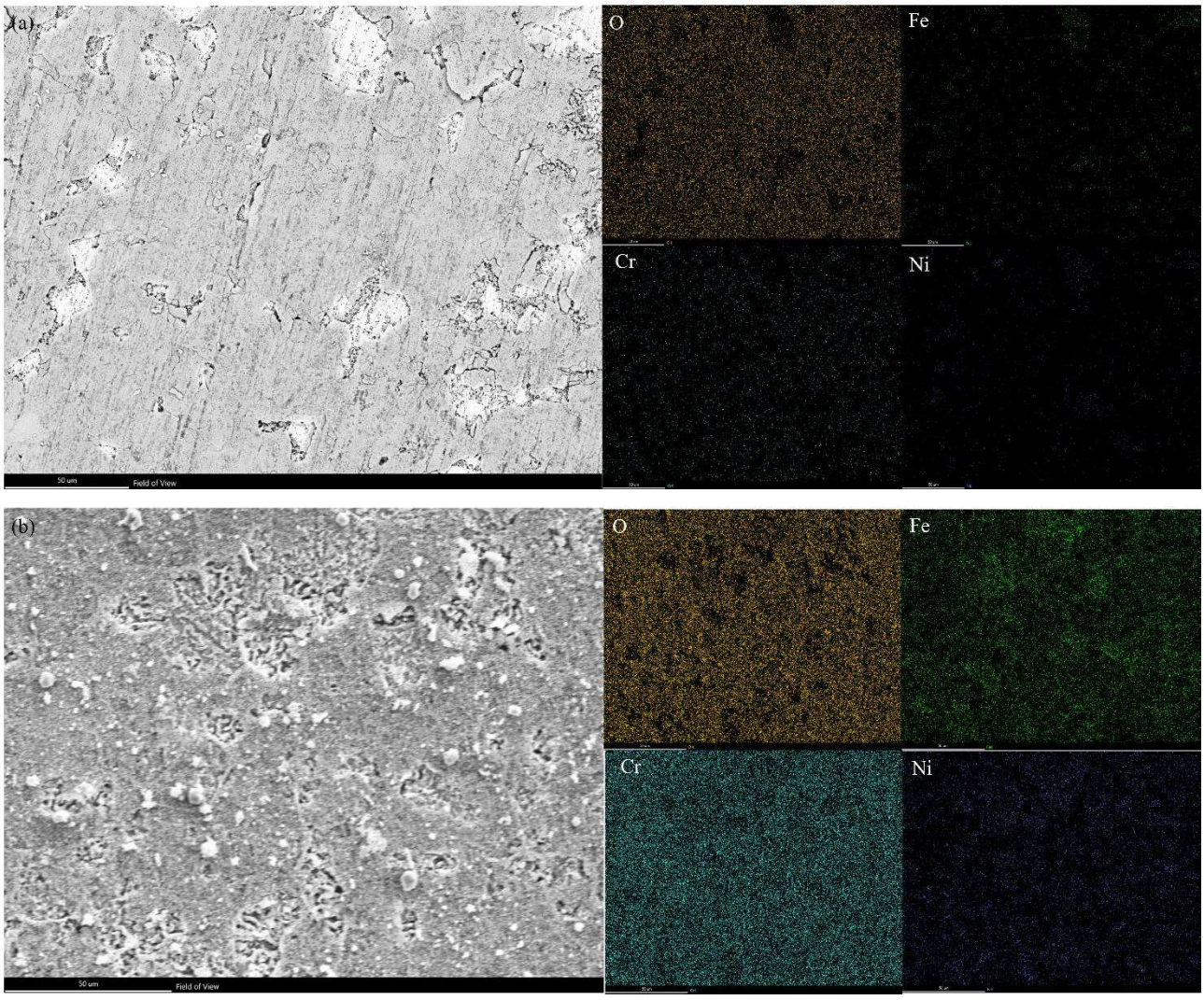

Fig. 7. The surface morphologies of the 316 SS alloy immersed in chloride salts at 650 ℃ for 72 h. (a) The 316 SS alloy immersed in salt 1; (b) The 316 SS alloy immersed in salt 2.

3.3 Effect of O and Cl adsorption on 316 SS alloy

3.3.1 Energies and structural properties of O and Cl atoms on the surface of the 316 SS alloy

To better understand the adsorption effects of O and Cl atoms on the 316 SS alloy, we simplified the structure of the adsorbate. This study focuses on the adsorption of O and Cl atoms on the (1 1 0) surface of the 316 SS alloy. The (1 1 0) surface is particularly significant because it is the most densely packed low-index surface in the body-centered cubic (BCC) structure, characterized by having the lowest surface energy. This feature makes it more likely to be exposed in practical applications [31, 69]. The adsorption energy, E_ads, of the adsorbates (O, Cl) is defined as [70, 71]:

$$E_{ad} = E_{ads} + E_{sub} - E_{ads/sub} \quad (4)$$

in which, E_{ads} is the total energy of the adsorbate, E_{sab} is the relaxed 316 SS alloy slab and $E_{ads/sub}$ is the slab covered with adsorbates.

According to this definition, the larger the adsorption energy, the stronger the interaction between the adsorbate and the substrate [72]. This section focuses on determining the adsorption energy of O and Cl atoms co-adsorbed on the surface of the 316 SS alloy. All adsorption energies are negative, indicating adsorption. For ease of comparison, the adsorption energies are taken as absolute values. The calculated adsorption energies are summarized in Table 2. It is worth noting that the co-adsorption energy when the coverage of O atoms and Cl atoms is 4/4 ML is significantly higher than when the coverage of O atoms and Cl atoms is 2/4 ML. This considerable co-adsorption energy is likely to due to the interaction of the adsorbate O atoms on the surface of 316 SS alloy. This further illustrates that adsorption on the surface of 316 SS alloy is not saturated. When the O atom coverage on the surface of the 316 SS alloy is 2/4 ML, additional O atoms need to be adsorbed to accelerate corrosion. The co-adsorption energy reflects the total adsorption energy of the reaction products of O and Cl on the surface of the 316 SS alloy. In general, the results of all adsorption structures and optimized configurations are closely related to the coverage of Cl and O atoms. As shown in Table 2,

the adsorption energies (Eads) of the configurations containing only O atoms or both O and Cl atoms are negative, indicating that these adsorption process are thermodynamically favorable.When comparing the three adsorption configurations, while the position and number of Cl atoms remain constant, the Eads value increases with higher O coverage. This suggests that the presence of O enhances the corrosion of the 316 SS alloy when immersed in molten chloride salts. Consequently, the significant co-adsorption energy can be attributed to the reactive interaction of the adsorbates on the surface of the 316 SS alloy.

The adsorbate layer, comprising Cl and O atoms, plays a critical role in influencing the surface work function, which quantifies the difficulty of electron escape from the substrate. The work functions of the clean 316 SS alloy (1 1 0) surface and the adsorbate (Cl and O)/316 SS alloy (1 1 0) system were determined through DFT calculations. The calculated surface work function of the clean 316 SS alloy (1 1 0) surface is 5.11 eV, as shown in Table 2.

Previous studies have reported calculated work functions for the 316 SS alloy (1 1 0) surface, ranging from 4.0 to 4.9 eV [73, 74]. Specifically, Ossowski et al. calculated the work function of clean Fe (1 1 0) as 4.77 eV, while Yin et al. obtained a value of 4.89 eV for the Fe (1 1 0) crystal plane under vacuum conditions [73, 74]. For the adsorbate (Cl and O)/316 SS alloy (1 1 0) system, the work functions were calculated to be 5.01 eV and 4.98 eV, respectively, under different coverages of Cl and O atoms, as shown in Table 2. These results indicate that the work function of the 316 SS alloy (1 1 0) surface decreases significantly after the co-adsorption of O and Cl atoms. Furthermore, as the coverage of O atoms increases, the work function of the adsorbate/316 SS alloy (1 1 0) system exhibits a slight decrease.

Table 2. Adsorption energies of the adsorbates O and Cl on 316 SS alloy (1 1 0) surface.

O coverage	Cl coverage	Adsorption energy of Cl and O |ΔE|	Work function
ML	ML	eV	eV
0	0	/	5.11
2/4	3/3	3.08	5.01
4/4	3/3	3.81	4.98

Moreover, the structures presented in Fig. 8 illustrate the optimized co-adsorption configurations of O atoms at a coverage of 2/4 ML and of Cl atoms. The co-adsorption behavior of O and Cl atoms is examined in these structures. For all configurations analyzed, the lateral movements of the relaxed atoms are negligible, with the predominant variations in atomic positions occurring in the z-direction [75]. The geometric parameters of the optimized structures are summarized in Table 3.

Our calculations reveal that, in the system with 4/4 ML O atom coverage, the minimum distance between the alloy's Fe-Cr-Ni atoms and the corrosive O-Cl atoms is approximately 1.649 Å. This distance is significantly smaller than that observed in the system with 2/4 ML O atom coverage. In summary, the results for all adsorption structures and their optimized configurations are closely related to the coverage of O atoms. The distance between the metal atoms (M, representing Fe, Cr, and Ni) and O-Cl indicates the strength of the interaction between the adsorbates and the surface.

From the analysis of the M(FeCrNi)—O-Cl distances with varying O coverage, it can be inferred that the interaction between O and the surface is stronger than that between Cl and the surface. Furthermore, in the co-adsorption optimized structure, the M(FeCrNi)—O distance is slightly smaller than the M(FeCrNi)—Cl distance. This suggests that the presence of O atoms in the corrosive environment facilitates electron transfer on the alloy surface, thereby enhancing the

corrosion process.

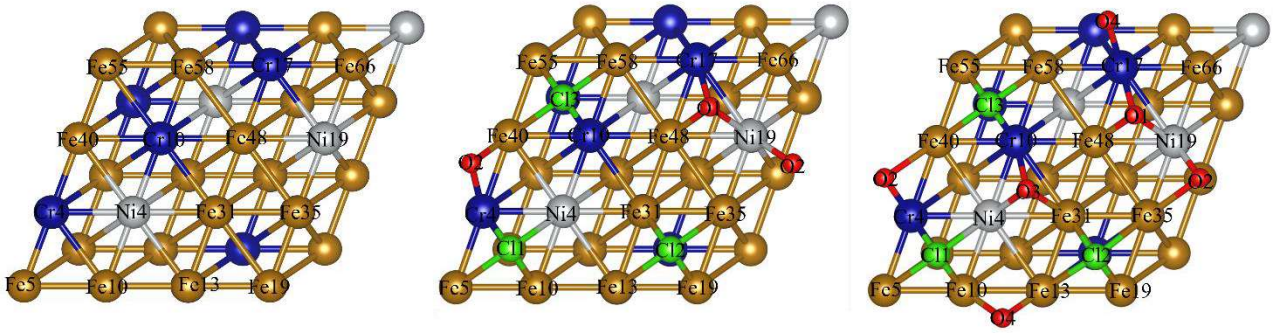

Pure 316 SS | 2/4 and 3/3 Cl 316 SS | 4/4 and 3/3 Cl 316 SS

Fig. 8. The top view of adsorbed structures of Cl and O atoms on 316 SS alloy (1 1 0) surfaces.

Table 3. The distance of adsorbed structures of Cl and O atoms on 316 SS alloy (1 1 0) surfaces in Fig. 9.

Coverage (ML)	Bonds	Distance (Å)	Coverage (ML)	Bonds	Distance (Å)
	/	/			
O 2/4 and Cl 3/3	O1-Cr17	1.936	O 4/4 and Cl 3/3	O1-Cr17	1.830
	O1-Fe48	1.942		O1-Fe48	1.779
	O1-Ni9	1.956		O1-Ni9	1.793
	O2-Cr4	1.961		O2-Cr4	1.688
	O2-Fe40	1.915		O2-Fe40	2.151
	O2-Ni9	1.982		O2-Ni9	1.649
	Cl1-Cr4	1.999		Cl1-Cr4	1.926
	Cl1-Fe5	2.451		Cl1-Fe5	2.317
	Cl1-Fe10	1.999		Cl1-Fe10	1.869
	Cl1-Ni4	2.403		Cl1-Ni4	2.372
	Cl2-Fe13	2.436		Cl2-Fe13	2.318
	Cl2-Fe31	2.013		Cl2-Fe31	1.980
	Cl2-Fe35	2.437		Cl2-Fe35	2.395

Cl2-Fe19	2.007	Cl2-Fe19	1.842
Cl3-Fe40	2.436	Cl3-Fe40	2.336
Cl3-Fe55	2.007	Cl3-Fe55	1.896
Cl3-Fe58	2.437	Cl3-Fe58	2.370
Cl3-Cr10	2.013	Cl3-Cr10	1.920

395

396 3.3.2 Electronic structure of O and Cl atoms on the 316 SS alloy (1 1 0) surface

397 According to the definition of adsorption energy, the higher the adsorption energy, the stronger
398 the interaction between the adsorbate and the substrate. Therefore, the interactions between
399 different atoms was studied in this paper. The difference in charge density (PDOS) can be defined in
400 Eq. (5):

401 $$\Delta\rho=\rho_{ads/slab}-\rho_{slab}-\rho_{ads} \quad (5)$$

402 Where $\rho_{ads/slab}$ represents the charge density of the adsorption system, ρ_{slab} represents the charge
403 density of the alloy surface, and ρ_{ads} represents the charge density of the adsorbed O and Cl atoms.

404 The difference in charge density and Bader charge analysis (representing the charge difference
405 after bonding) can effectively characterize the charge transfer between atoms [76]. In this study, we
406 calculate the p orbitals of Cl and O atoms, as well as PDOS of the alloy directly interacting with
407 these atoms, with the results illustrated in Fig. 9.

408 To demonstrate the electronic interactions between adsorbates and the 316 SS (1 1 0) surface, the
409 PDOS for O and Cl atoms in co-adsorbed configurations at coverages of 2/4 ML and 4/4 ML was
410 calculated, as well as the DOS for the alloy atoms themselves. These results are presented in Fig. 9.
411 When the O coverage is 2/4 and 4/4 ML, the O and Cl peaks resonate with the surface FeCrNi peaks,
412 indicating a strong interaction between these adsorbates and the alloy surface. Notably, at 4/4 ML

coverage, the states of the O atoms show a downward shift in peak position, signifying a shift in electronic energy levels. This shift in peak position suggests that the O-Cl (4/4-3/3 ML) adsorption surface has a stronger interaction with the alloy than the O (2/4-3/3 ML) adsorption surface. Therefore, it can be concluded that higher O coverage enhances the surface interactions of the 316 SS alloy, which is consistent with the previous results on geometric parameters and adsorption energy.

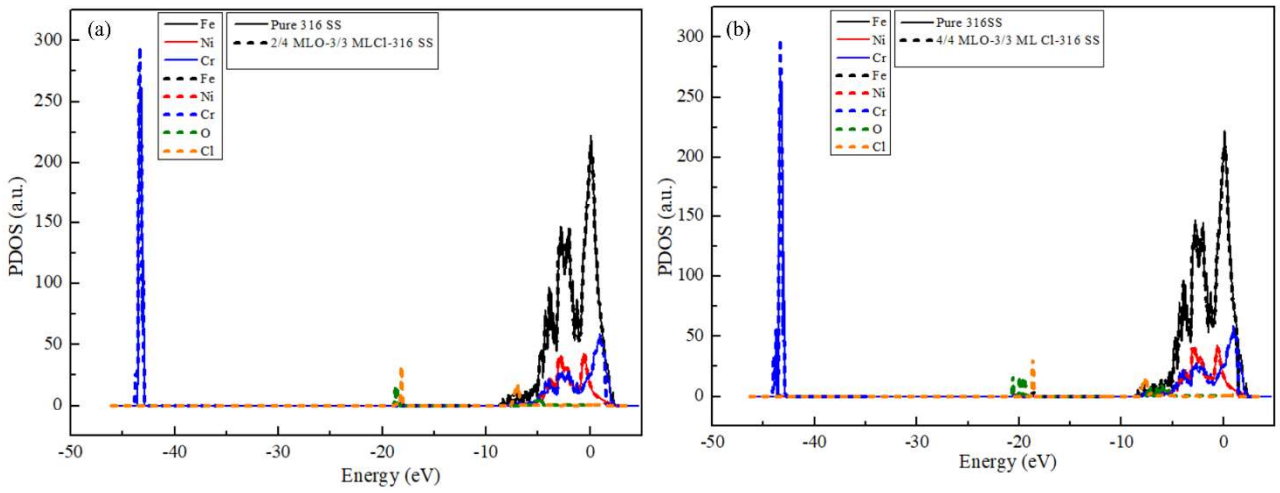

Fig. 9. The PDOS results of different coverage Cl and O adsorbed 316 SS alloy (1 1 0) surface.

A detailed electronic analysis was conducted to further investigate the effects of the reaction between Cl and O atoms on the surface of the 316 SS alloy. Fig. 10 illustrates the differential charge density of the 316 SS alloy. The results shown in Fig. 10(a) indicate that the adsorption of Cl atoms on the surface of the 316 SS alloy enhances the charge transfer of O atoms while simultaneously suppressing the charge transfer associated with the Cl atom. Fig. 10(b) reveals that charge transfer occurs both on the surface and in the subsurface regions of the 316 SS alloy. Specifically, as the number of O atoms adsorbed on the surface increases in the presence of Cl, the amount of charge transfer also increases, suggesting a more pronounced corrosion phenomenon. Table 4 summarizes the specific data related to the adsorption of adsorbates on the surface of the 316 SS alloy and the

corresponding charge transfer amounts. The simulation results show that the charge transfer of O is greater than that of Cl. Compared to Cl, O is preferentially adsorbed on the alloy surface. This finding supports the conclusion that Cl atoms accelerate the corrosion of the 316 SS alloy. Furthermore, the charge transfer in the 316 SS alloy follows the order: Ni > Fe > Cr. This suggests that the oxidation sequence in the molten salt environment is Cr, followed by Fe, and then Ni. This observation is consistent with the results of the Gibbs free energy calculations presented in Table 5.

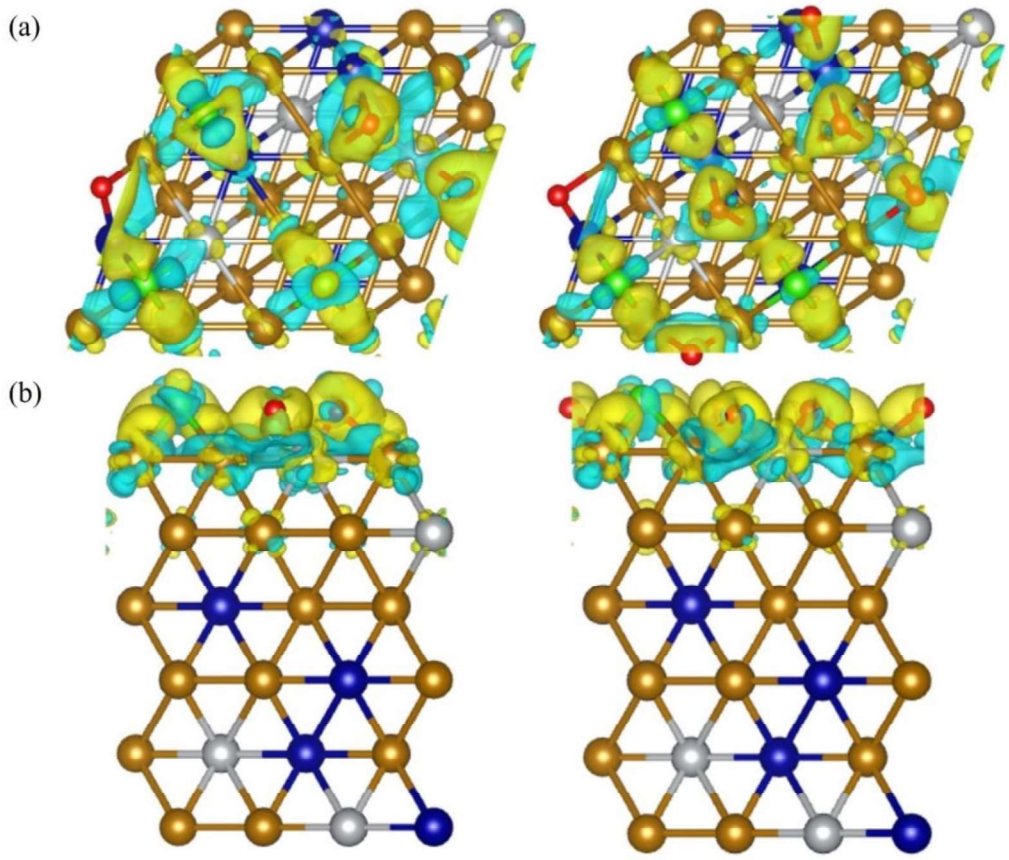

Fig. 10. Adsorption of Cl and different coverage O of the 316 SS alloy charge density difference diagram. (a) The upper panel is a top view; (b) The lower panel is a side view

443 **Table 4.** Charge transfer amount of the 316 SS alloy surface and subsurface.

	Atom	O 2/4 and Cl 3/3	O 4/4 and Cl 3/3
Adsorbates	O1	-0.87	-0.88
	O2	-0.86	-0.86
	O3	/	-0.89
	O4	/	-0.87
	Cl1	-0.46	-0.43
	Cl2	-0.46	-0.41
	Cl3	-0.49	-0.48
Surface	Fe5	0.06	0.07
	Fe10	0.04	0.26
	Fe13	0	0.26
	Fe19	0.08	0.07
	Fe31	0.05	0.21
	Fe35	0.13	0.19
	Fe40	0.25	0.26
	Fe48	0.06	0.06
	Fe55	0.06	0.06
	Fe58	0	0.06
	Fe66	0.06	0.07
	Cr4	0.79	0.84
	Cr10	0.55	0.73
	Cr17	0.64	0.85
	Ni9	0	0.11

Ni14	0.12	0.22

Table 5. The redox reaction of Ni, Fe, and Cr at 650 °C. The standard Gibbs free energy Δ_rG^0 of the reaction was estimated using the chemical database (6.0).

Reaction	Δ_rG^0 ((kJ/mol))
$4Cr+3O_2(g)=2Cr_2O_3$	-1781.35
$4Fe+3O_2(g)=2Fe_2O_3$	-1156.64
$2Ni+O_2(g)=2NiO$	-310.54

4. Conclusions

In this paper, experimental methods and density functional theory (DFT) calculations were employed to investigate the effect of oxygen (O) in molten salt on the surface of the 316 SS alloy. The experimental approach focused on analyzing the microstructure and chemical properties of the alloy after corrosion, while the DFT method examined the adsorption energy, structural properties, and electronic properties of O and Cl interacting on the (1 1 0) surface of the 316 SS alloy. The main conclusions are as follows:

(1) Localized corrosion occurs on the surface of the 316 SS alloy exposed to salt 1. However, when the 316 SS alloy is immersed in salt 2, which has a higher oxygen content, oxidation penetrates more deeply into the alloy matrix. Additionally, pits form on the surface of the alloy immersed in salt 2, resulting in the formation of a thin oxide film composed of polyhedral spinels. XPS valence state analysis reveals that the primary oxidation product is Cr_2O_3, regardless of the oxygen content in the molten salt environment. Furthermore, the oxide layer formed on the surface of the 316 SS alloy immersed in salt 1 is much thinner, leading to a significantly lower Cr_2O_3 content compared to the alloy immersed in salt 2.

(2) DFT calculation results indicate that the content of O atoms influences the corrosion behavior

of the 316 SS alloy surface. The O content in the molten salt significantly accelerates the corrosion of the 316 SS alloy surface. As the concentration of O atoms increases, subsurface damage to the 316 SS alloy intensifies. Furthermore, charge transfer in the 316 SS alloy follows the order of Ni > Fe > Cr. This suggests that the oxidation sequence in the molten salt environment is Cr, followed by Fe, and then Ni. The interaction between Cr and O is strongest on the surface of the 316 SS alloy, which aligns with the experimental results.

Acknowledgements

This work was financially supported by the National Natural Science Foundation of China (Grant No. 52130607, 52090062 and 52211530087) and the Double First-Class Key Program of Gansu Provincial Department of Education (Grant No. GCJ2022-38).

Appendix A. Supplementary data

Supplementary data to this article can be found in **Appendix A**.

References

[1] J. Gomez-Vidal, R. Tirawat, Corrosion of alloys in a chloride molten salt (NaCl-LiCl) for solar thermal technologies, Solar Energy Materials and Solar Cells 157 (2016) 234-244, https://doi.org/10.1016/j.solmat.2016.05.052

[2] X. Montero, A. Ishida, T. Meißner, H. Murakami, M. Galetz, Effect of surface treatment and crystal orientation on hot corrosion of a Ni-based single-crystal superalloy, Corrosion Science 166 (2020) 108472, https://doi.org/10.1016/j.corsci.2020.108472

[3] P. Zhang, X. Li, J. Moverare, R. Lin Peng, The iron effect on hot corrosion behaviour of MCrAlX coating in the presence of NaCl at 900 °C, Journal of Alloys and Compounds 815 (2020) 152381, https://doi.org/10.1016/j.jallcom.2019.152381

[4] B. Wei, C. Chen, J. Xu, L. Yang, Y. Jia, Y. Du, M. Guo, C. Sun, Z. Wang, F. Wang, Comparing the hot corrosion of (100), (210) and (110) Ni-based superalloys exposed to the mixed salt of Na2SO4-NaCl at 750 °C: Experimental study and first-principles calculation, Corrosion Science 195 (2022) 109996, https://doi.org/10.1016/j.corsci.2021.109996

[5] Y. Li, Y. Ouyang, R. Fang, X. Jiang, Z. Xie, L. Wu, J. Long, C. Zhong, A nickel-underlayer/LDH-midlayer/siloxane-toplayer composite coating for inhibiting galvanic corrosion between Ni layer and Mg alloy, Chemical Engineering Journal 430 (2022) 132776, https://doi.org/10.1016/j.cej.2021.132776

[6] Y. Zhang, N. Li, N. Ling, J. Zhang, L. Wang, Enhanced long-term corrosion resistance of Mg alloys by superhydrophobic and self-healing composite coating, Chemical Engineering Journal 449 (2022) 137778, https://doi.org/10.1016/j.cej.2022.137778

[7] S. Yang, R. Sun, K. Chen, Self-healing performance and corrosion resistance of phytic acid/cerium composite coating on microarc-oxidized magnesium alloy, Chemical Engineering Journal 428 (2022) 131198, https://doi.org/10.1016/j.cej.2021.131198

[8] J. Wei, B. Li, L. Jing, N. Tian, X. Zhao, J. Zhang, Efficient protection of Mg alloy enabled by combination of a conventional anti-corrosion coating and a superamphiphobic coating, Chemical Engineering Journal 390 (2020) 124562, https://doi.org/10.1016/j.cej.2020.124562

[9] B. Su, B. Wang, L. Luo, L. Wang, B. Li, C. Liu, Y. Su, Y. Xu, H. Huang, J. Guo, H. Fu, Y. Zou, Tuning microstructure and improving the corrosion resistance of Ti-6Al-3Nb-2Zr-1Mo alloy using

506 the electron beam freeform fabrication, Chemical Engineering Journal 444 (2022) 136524,
507 https://doi.org/10.1016/j.cej.2022.136524
508 [10] S. Masoud Emarati, M. Mozammel, Theoretical, fundamental and experimental study of Liquid-
509 repellency and corrosion resistance of fabricated superamphiphobic surface on Al alloy 2024,
510 Chemical Engineering Journal 387 (2020) 124046, https://doi.org/10.1016/j.cej.2020.124046
511 [11] B. Zhang, J. Wang, B. Wu, X.W. Guo, Y.J. Wang, Unmasking chloride attack on the passive film
512 of metals,
513 [12] H. Li, E. Zhou, Y. Ren, D. Zhang, D. Xu, C. Yang, H. Feng, Z. Jiang, X. Li, T. Gu, K. Yang,
514 Investigation of microbiologically influenced corrosion of high nitrogen nickel-free stainless steel by
515 Pseudomonas aeruginosa, Corrosion Science 111 (2016) 811-821,
516 https://doi.org/10.1016/j.corsci.2016.06.017
517 [13] S. Zhang, H. Li, Z. Jiang, B. Zhang, Z. Li, J. Wu, H. Feng, H. Zhu, F. Duan, Chloride- and
518 sulphate-induced hot corrosion mechanism of super austenitic stainless steel S31254 under dry gas
519 environment, Corrosion Science 163 (2020) 108295, https://doi.org/10.1016/j.corsci.2019.108295
520 [14] L. Guo, Q. Liu, H. Yin, T.J. Pan, Z. Tang, Excellent corrosion resistance of 316 stainless steel in
521 purified NaCl-MgCl2 eutectic salt at high temperature, Corrosion Science 166 (2020) 108473,
522 https://doi.org/10.1016/j.corsci.2020.108473
523 [15] B. Liu, X. Wei, W. Wang, J. Lu, J. Ding, Corrosion behavior of Ni-based alloys in molten NaCl-
524 CaCl2-MgCl2 eutectic salt for concentrating solar power, Solar Energy Materials and Solar Cells 170
525 (2017) 77-86, https://doi.org/10.1016/j.solmat.2017.05.050
526 [16] W. Ding, H. Shi, Y. Xiu, A. Bonk, A. Weisenburger, A. Jianu, T. Bauer, Hot corrosion behavior
527 of commercial alloys in thermal energy storage material of molten MgCl2/KCl/NaCl under inert

528 atmosphere, Solar Energy Materials and Solar Cells 184 (2018) 22-30,
529 https://doi.org/10.1016/j.solmat.2018.04.025
530 [17] F. Gesmundo, D.J. Young, S.K. Roy, The High Temperature Corrosion of Metals in Sulfidizing-
531 Oxidizing Environments: A Critical Review, 8(3) (1989) 149-190,
532 https://doi.org/10.1515/HTMP.1989.8.3.149
533 [18] W. Su, S. Niu, Y. Huang, C. Wang, Y. Wen, X. Li, C. Deng, C. Deng, M. Liu, Friction and wear
534 properties of plasma-sprayed Cr2O3–BaCrO4 coating at elevated temperatures, Ceramics
535 International 48(6) (2022) 8696-8705, https://doi.org/10.1016/j.ceramint.2021.12.081
536 [19] F. Mansfeld, N.E. Paton, W.M. Robertson, The high temperature behavior of superalloys exposed
537 to sodium chloride: II. corrosion, Metallurgical Transactions 4(1) (1973) 321-327,
538 https://doi.org/10.1007/BF02649632
539 [20] W. Zhou, Y. Yang, G. Zheng, K.B. Woller, P.W. Stahle, A.M. Minor, M.P. Short, Proton
540 irradiation-decelerated intergranular corrosion of Ni-Cr alloys in molten salt, Nature Communications
541 11(1) (2020) 3430, http://dx.doi.org/10.1038/s41467-020-17244-y
542 [21] M. Sarvghad, S. Delkasar Maher, D. Collard, M. Tassan, G. Will, T.A. Steinberg, Materials
543 compatibility for the next generation of Concentrated Solar Power plants, Energy Storage Materials
544 14 (2018) 179-198, https://doi.org/10.1016/j.ensm.2018.02.023
545 [22] H. Li, X. Wang, X. Yin, X. Yang, J. Tang, J. Gong, Corrosion and electrochemical investigations
546 for stainless steels in molten Solar Salt: The influence of chloride impurity, Journal of Energy Storage
547 39 (2021) 102675, https://doi.org/10.1016/j.est.2021.102675
548 [23] S. Rong, L. Huang, R. Wang, J. Xu, Z. Peng, Y. Chen, H. Jin, L. Guo, Corrosion behaviors of
549 Ni-based and Fe-based alloys in supercritical water gasification with inorganic chloride salt,

Corrosion Science 219 (2023) 111241, https://doi.org/10.1016/j.corsci.2023.111241

[24] M. Wu, J. Shi, Beneficial and detrimental impacts of molybdate on corrosion resistance of steels in alkaline concrete pore solution with high chloride contamination, Corrosion Science 183 (2021) 109326, https://doi.org/10.1016/j.corsci.2021.109326

[25] G.C. Fryburg, F.J. Kohl, C.A. Stearns, W.L. Fielder, Chemical Reactions Involved in the Initiation of Hot Corrosion of B-1900 and NASA-TRW VIA, Journal of The Electrochemical Society 129(3) (1982) 571, https://doi.org/10.1149/1.2123928

[26] R. Serrano-López, J. Fradera, S. Cuesta-López, Molten salts database for energy applications, Chemical Engineering and Processing: Process Intensification 73 (2013) 87-102, https://doi.org/10.1016/j.cep.2013.07.008

[27] Y. Zhang, S. Sanvito, Atomistic simulations of surface reactions in ultra-high-temperature ceramics: O2, H2O and CO adsorption and dissociation on ZrB2(0001) surfaces, Applied Surface Science 566 (2021) 150622, https://doi.org/10.1016/j.apsusc.2021.150622

[28] M.A. Murmura, M. Sheintuch, Permeance inhibition of Pd-based membranes by competitive adsorption of CO: Membrane size effects and first principles predictions, Chemical Engineering Journal 347 (2018) 301-312, https://doi.org/10.1016/j.cej.2018.04.072

[29] G. Jiang, D. Xu, Y. Wei, H. Liu, L. Liu, W. Kuang, Corrosion of Zircaloy-4, Zr-1Nb and FeCrAl alloys in deaerated water at 330 °C and 14 MPa: Superior corrosion resistance and corrosion mechanism of FeCrAl alloy by experiments and molecular dynamics simulations, Chemical Engineering Journal 462 (2023) 142143, https://doi.org/10.1016/j.cej.2023.142143

[30] Y. He, X. Zhao, C. Chen, H. Yu, First principles molecular dynamics simulations of H2S dissociation on Fe (111) in aqueous environments, Applied Surface Science 554 (2021) 149618,

https://doi.org/10.1016/j.apsusc.2021.149618

[31] X. Li, Y. Ma, W. Zhou, Z. Liu, Spin-polarized DFT calculations of elemental effects on hydrogen atom adsorption on FeCrAl (110) surface, Applied Surface Science 581 (2022) 152273, https://doi.org/10.1016/j.apsusc.2021.152273

[32] M. Hao, W. Zeng, Adsorption mechanism of sulphide gas molecules on γ-Fe(1 1 1) surface: A density functional theory study, Applied Surface Science 563 (2021) 150376, https://doi.org/10.1016/j.apsusc.2021.150376

[33] Y. Wang, X. Hu, T. Guo, W. Tian, J. Hao, Q. Guo, The competitive adsorption mechanism of CO2, H2O and O2 on a solid amine adsorbent, Chemical Engineering Journal 416 (2021) 129007, https://doi.org/10.1016/j.cej.2021.129007

[34] C. Qin, Y. Jiang, J. Zhou, X. Song, Z. Liu, D. Li, F. Zhou, Y. Xie, C. Xie, Effect of supercritical CO2 extraction on CO2/CH4 competitive adsorption in Yanchang shale, Chemical Engineering Journal 412 (2021) 128701, https://doi.org/10.1016/j.cej.2021.128701

[35] W. Liu, J. Sun, C. Ye, The influence of tensile strain on water adsorbed on Fe (100) surface: Surface chemistry aspect of stress corrosion cracking, Applied Surface Science 481 (2019) 192-199, https://doi.org/10.1016/j.apsusc.2019.03.029

[36] F. Liu, X. Ding, J. Sun, Surface relaxation and initial surface corrosion of strained Mo(100) surface, Applied Surface Science 586 (2022) 152648, https://doi.org/10.1016/j.apsusc.2022.152648

[37] L. Zhao, J. Wang, L. Cui, B. Li, X. Du, H. Wu, Performance design of high-temperature chloride salts as thermal energy storage material, Journal of Thermal Science 33 (2024) 479–490. https://doi.org/10.1007/s11630-024-1921-4

[38] L. Zhao, K. Jiang, L. Cui, X. Du, H. Wu, Influence of alkaline earth metal CaCl2 on early-stage

corrosion behavior of 316 stainless steel in high-temperature molten salt, Journal of Energy Storage, 98 (2024) 113034. https://doi.org/10.1016/j.est.2024.113034.

[39] G. Kresse, J. Furthmüller, Efficient iterative schemes for ab initio total-energy calculations using a plane-wave basis set, Physical Review B - Condensed Matter and Materials Physics 54(16) (1996) 11169-11186, https://doi.org/10.1103/PhysRevB.54.11169

[40] G. Kresse, J. Furthmüller, Efficient iterative schemes for ab initio total-energy calculations using a plane-wave basis set, Physical review. B, Condensed matter 54(16) (1996) 11169-11186, https://doi.org/10.1103/physrevb.54.11169

[41] P.E. Blöchl, Projector augmented-wave method, Physical Review B 50(24) (1994) 17953-17979, https://doi.org/10.1103/PhysRevB.50.17953

[42] G. Kresse, From ultrasoft pseudopotentials to the projector augmented-wave method, Physical Review B - Condensed Matter and Materials Physics 59(3) (1999) 1758-1775, https://doi.org/10.1103/PhysRevB.59.1758

[43] J. KLIMEŠ, D. Bowler, A. Michaelides, Van der Waals density functionals applied to solids, Physical Review B, 83 (2011) 195131. https://doi.org/10.1103/PhysRevB.83.195131.

[44] J. Klimeš, D. Bowler, A. Michaelides, Chemical accuracy for the van der Waals density functional. Journal of Physics: Condensed Matter, 22 (2010) 022201. https://doi.org/10.1088/0953-8984/22/2/022201

[45] S. Grimme, J. Antony, S. Ehrlich, H. Krieg, A consistent and accurate ab initio parametrization of density functional dispersion correction (DFT-D) for the 94 elements H-Pu, The Journal of Chemical Physics 132(15) (2010), https://doi.org/10.1063/1.3382344

[46] C. DellaRovere, J. Alano, R. Silva, Characterization of passive films on shape memory stainless

steels, Corrosion Science 57 (2012) 154-161, https://doi.org/10.1016/j.corsci.2011.12.022

[47] Q. Liu, Z. Wang, W. Liu, H. Yin, Z. Tang, Y. Qian, Ni-Mo-Cr alloy corrosion in molten NaCl-KCl-MgCl2 salt and vapour, Corrosion Science 180 (2021) 109183, https://doi.org/10.1016/j.corsci.2020.109183

[48] P. Wang, K. Du, M. Tang, H. Yin, D. Wang, Chloride impurity induced corrosion of nickel anode and its protection in molten Li2CO3-Na2CO3-K2CO3, Corrosion Science 196 (2022) 110027, https://doi.org/10.1016/j.corsci.2021.110027

[49] H. Ai, M. Shen, H. Sun, K.P. Dolan, C. Wang, M. Ge, H. Yin, X. Li, H. Peng, N. Li, L. Xie, Effects of O2− additive on corrosion behavior of Fe–Cr–Ni alloy in molten fluoride salts, Corrosion Science 150 (2019) 175-182, https://doi.org/10.1016/j.corsci.2019.01.040

[50] T. Ghaznavi, M. Bryk, S. Persaud, R. Newman, Alloying effects in high temperature molten salt corrosion, Corrosion Science 197 (2022) 110003, https://doi.org/10.1016/j.corsci.2021.110003

[51] Y. Wang, C. Liu, Z. Jiao, L. Cai, C. Sun, D. Wang, L. Cui, C. Wen, R. Zeng, Corrosion behavior and mechanical property of Mg-4Li-1Ca alloys under micro-compressive stress, Journal of Materials Science & Technology 175 (2024) 170-184, https://doi.org/10.1016/j.jmst.2023.08.019

[52] W. Ci, X. Chen, X. Dai, C. Liu, Y. Ma, D. Zhao, F. Pan, Achieving ultra-high corrosion-resistant Mg-Zn-Sc alloys by forming Sc-assisted protective corrosion product film, Journal of Materials Science & Technology 181 (2024) 138-151, https://doi.org/10.1016/j.jmst.2023.08.068

[53] V. D'Ippolito, G. Andreozzi, D. Bersani, P. Lottici, Raman fingerprint of chromate, aluminate and ferrite spinels, 46(12) (2015) 1255-1264, https://doi.org/10.1002/jrs.4764

[54] G. Jiang, L. Liu, D. Xu, H. Liu, M. Wang, J. Yang, Effect of dissolved precursors on corrosion characteristics of Ni-based alloy Inconel 625, stainless steel 316L and titanium alloy TA2 in acidic

638 and neutral supercritical water: A comparative study, The Journal of Supercritical Fluids 209 (2024)
639 106249, https://doi.org/10.1016/j.supflu.2024.106249
640 [55] M. Fulger, D. Ohai, M. Mihalache, M. Pantiru, V. Malinovschi, Oxidation behavior of Incoloy
641 800 under simulated supercritical water conditions, Journal of Nuclear Materials 385(2) (2009) 288-
642 293, https://doi.org/10.1016/j.jnucmat.2008.12.004
643 [56] Z. Zhang, J. Wang, E.-H. Han, W. Ke, Analysis of Surface Oxide Films Formed in Hydrogenated
644 Primary Water on Alloy 690TT Samples With Different Surface States, Journal of Materials Science
645 & Technology 30(12) (2014) 1181-1192, https://doi.org/10.1016/j.jmst.2014.09.002
646 [57] K. Choudhry, D. Guzonas, D. Kallikragas, I. Svishchev, On-line monitoring of oxide formation
647 and dissolution on alloy 800H in supercritical water, Corrosion Science 111 (2016) 574-582,
648 https://doi.org/10.1016/j.corsci.2016.05.042
649 [58] J. Wang, S. Zhang, F. Han, Y. Luo, J. Chen, Z. Hu, Z. Pan, M. Hu, Corrosion performance and
650 mechanisms of tantalum coatings on 316 stainless-steel in subcritical aqueous solutions of NaCl and
651 NaBr, Corrosion Science 231 (2024) 112006, https://doi.org/10.1016/j.corsci.2024.112006
652 [59] B. Tan, K. Klabunde, P. Sherwood, X-ray photoelectron spectroscopy studies of solvated metal
653 atom dispersed catalysts. Monometallic iron and bimetallic iron-cobalt particles on alumina,
654 Chemistry of Materials 2(2) (1990) 186-191, https://doi.org/10.1021/cm00008a021
655 [60] J.C. Langevoort, I. Sutherland, L. Hanekamp, P.J. Gellings, On the oxide formation on stainless
656 steels AISI 304 and incoloy 800H investigated with XPS, Applied Surface Science 28(2) (1987) 167-
657 179, https://doi.org/10.1016/0169-4332(87)90062-6
658 [61] G. Allen, S. Harris, J. Jutson, J. Dyke, A study of a number of mixed transition metal oxide
659 spinels using X-ray photoelectron spectroscopy, Applied Surface Science 37(1) (1989) 111-134,

https://doi.org/10.1016/0169-4332(89)90977-X

[62] Y. Yang, C. Zhang, Y. Peng, Y. Yu, L. Liu, Effects of crystallization on the corrosion resistance of Fe-based amorphous coatings, Corrosion Science 59 (2012) 10-19, https://doi.org/10.1016/j.corsci.2012.02.003

[63] H. Wang, Y. Cheng, Y. Wan, N. Jeyaprakash, Y. Wang, K. Ma, J. Yang, Influence of scanning speed on microstructure and corrosion resistance of Fe-based amorphous coatings by high-speed laser cladding, Surface and Coatings Technology 479 (2024) 130449, https://doi.org/10.1016/j.surfcoat.2024.130449

[64] Z. Wang, C. Carrière, A. Seyeux, S. Zanna, D. Mercier, P. Marcus, XPS and ToF-SIMS Investigation of Native Oxides and Passive Films Formed on Nickel Alloys Containing Chromium and Molybdenum, Journal of The Electrochemical Society 168(4) (2021) 041503, https://doi.org/10.1149/1945-7111/abf308

[65] L. Ma, E. Pascalidou, F. Wiame, S. Zanna, V. Maurice, P. Marcus, Passivation mechanisms and pre-oxidation effects on model surfaces of FeCrNi austenitic stainless steel, Corrosion Science 167 (2020) 108483, https://doi.org/10.1016/j.corsci.2020.108483

[66] A. Muñoz, T. Meyer, D. Schild, W. Calvet, Early stages of corrosion of stainless steel 309 S in geological brines studied by sychrotron radiation photoelectron spectroscopy, Corrosion Science 212 (2023) 110934, https://doi.org/10.1016/j.corsci.2022.110934

[67] B. Li, S. Chen, M. Xiao, Q. Tu, Z. Xu, T. Feng, Z. Zhang, Z. Yuan, C. Xu, L. Gong, X. Xi, W. Zhang, Preparation of Ni–Mo/GO composite coatings with strengthened mechanical properties and enhanced corrosion resistance, Surface and Coatings Technology 477 (2024) 130404, https://doi.org/10.1016/j.surfcoat.2024.130404

682 [68] H. Liu, D. Liu, X. Cheng, Z. Hua, S. He, One-step electrodeposition of Ni-Mo electrode with
683 column-pyramid hierarchical structure for highly-efficient hydrogen evolution, Materials & Design
684 224 (2022) 111427, https://doi.org/10.1016/j.matdes.2022.111427
685 [69] V. Sahni, J. Perdew, J. Gruenebaum, Variational calculations of low-index crystal face-dependent
686 surface energies and work functions of simple metals, Physical Review B 23(12) (1981) 6512-6523,
687 https://doi.org/10.1103/PhysRevB.23.6512
688 [70] D. Jiang, E. Carter, Adsorption and diffusion energetics of hydrogen atoms on Fe(110) from first
689 principles, Surface Science 547(1) (2003) 85-98, https://doi.org/10.1016/j.susc.2003.10.007
690 [71] D. Sorescu, First principles calculations of the adsorption and diffusion of hydrogen on Fe(100)
691 surface and in the bulk, Catalysis Today 105(1) (2005) 44-65,
692 https://doi.org/10.1016/j.cattod.2005.04.010
693 [72] J. Zhao, Y. Xu, S. Liu, X. Ding, The effect of oxygen-containing species on corrosion behavior
694 of Ta (110) surface: A DFT study with an experimental verification, Applied Surface Science 586
695 (2022) 152810, https://doi.org/10.1016/j.apsusc.2022.152810
696 [73] T. Ossowski, J. DaSilva, A. Kiejna, Water adsorption on the stoichiometric and defected Fe(110)
697 surfaces, Surface Science 668 (2018) 144-149, https://doi.org/10.1016/j.susc.2017.10.030
698 [74] X. Yin, H. Wang, E. Han, Effects of solvation and applied potential on the adsorption behaviors
699 of H, O, OH and H2O on Fe(110) surface, Surface Science 691 (2020) 121504,
700 https://doi.org/10.1016/j.susc.2019.121504
701 [75] X. Wei, C. Dong, Z. Chen, J. Huang, K. Xiao, X. Li, Insights into SO2 and H2O co-adsorption
702 on Cu (100) surface with calculations of density functional theory, Transactions of Nonferrous Metals
703 Society of China 25(12) (2015) 4102-4109, https://doi.org/10.1016/S1003-6326(15)64059-6

[76] G. Henkelman, A. Arnaldsson, H. Jónsson, A fast and robust algorithm for Bader decomposition of charge density, Computational Materials Science 36(3) (2006) 354-360, https://doi.org/10.1016/j.commatsci.2005.04.010